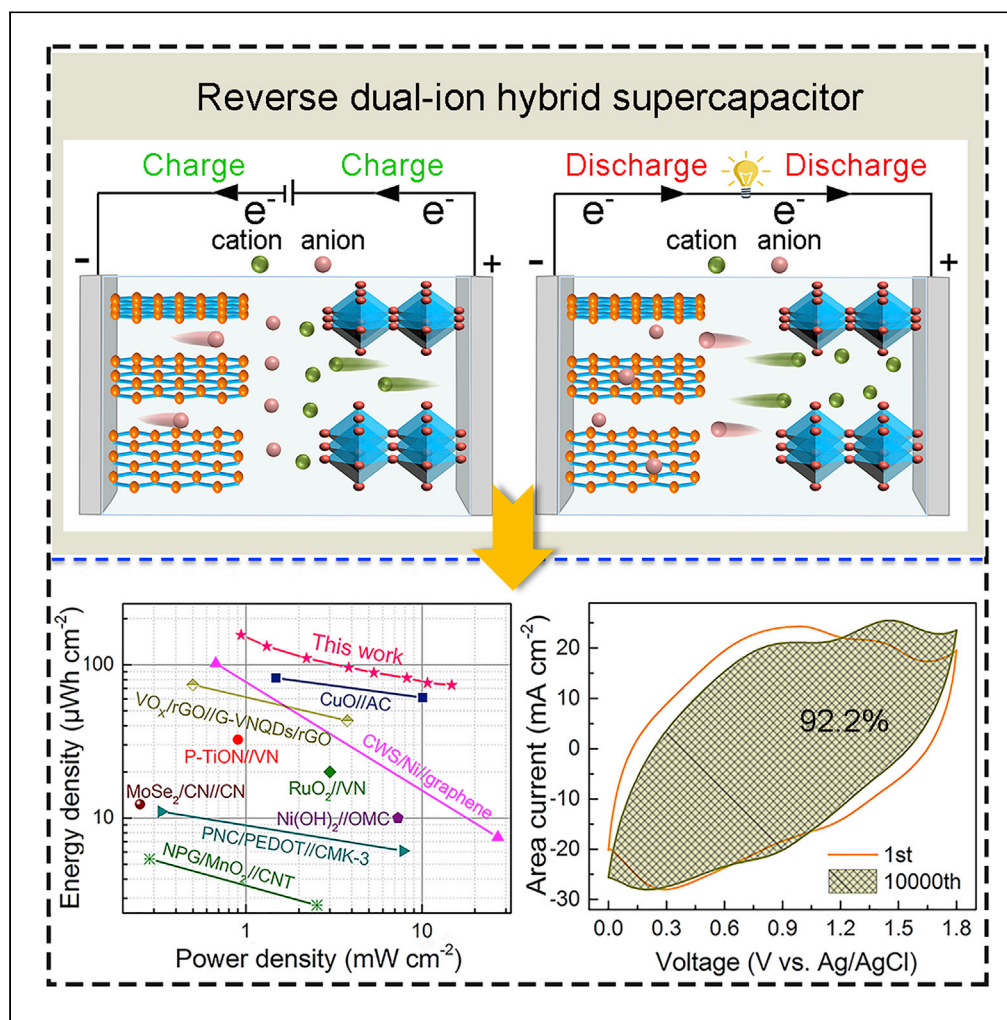**Article**

Mesoporous vanadium nitride as anion storage electrode for reverse dual-ion hybrid supercapacitor

Chenglong Shi, Junlong Sun, Faqi Ji, Wenjun Chen, Youyong Pang, Bo-Tian Liu

btliu2018@glut.edu.cn

Highlights

The MPs VN anode as anion storage material was firstly proposed

The dual-ion supercapacitors were firstly constructed by employing the MPs VN anode

The reverse storage mechanism was firstly applied to hybrid supercapacitors

Article

Mesoporous vanadium nitride as anion storage electrode for reverse dual-ion hybrid supercapacitor

Chenglong Shi,[1] Junlong Sun,[1] Faqi Ji,[1] Wenjun Chen,[1] Youyong Pang,[1] and Bo-Tian Liu[1,2,3,*]

SUMMARY

In traditional dual-ion systems, the cathode usually is employed as anion-storage materials. Herein, we propose a new dual-ion hybrid supercapacitor with reverse anion/cation-storage mechanism, consisting of a mesoporous (MPs) VN anode as a pivotal anion-storage material and $K_{2-x}Mn_8O_{16}$ nanosheet arrays grown on carbon cloth (NSs/CC) as (K-storage) cathode. During charge/discharge, the anode and cathode reversibly store/release OH^- ions and K^+ ions, respectively. Herein, the MPs VN as anion-storage electrode can operate in an alkaline condition and deliver a high capacitance of 251 mF cm^{-2} with desired low-voltage plateau. More importantly, benefiting from unique reverse dual-ion mechanism, the (MPs VN-$K_{2-x}Mn_8O_{16}$ NSs/CC) hybrid device displays excellent rate performance and satisfying area capacitance along with good durability of 92.2% after 10,000 cycles at a scan rate of 100 mV s^{-1}. It offers new ideas to expand the range of anion-storage materials in dual-ion hybrid supercapacitors.

INTRODUCTION

Supercapacitors based on cation or anion reversible reactions have been thoroughly studied over past several decades (Dunn et al., 2011; Saikia et al., 2020; Wang et al., 2012). However, it paid less attention to the simultaneous utilization of the cation and anion in previous studies (Muzaffar et al., 2019; Meng and Tang, 2018). And in fact, aqueous dual-ion battery (ADIB) has attracted intense increase because of their low cost, high safety, and durability Larcher and Tarascon (2015); Shao et al. (2018). Thus far, Zhang et al. described an ADIB employing *n*-type polyimide and p-type radical polymer reaction with anion and cations, respectively (Zhang et al., 2019). Yu et al. propose a $Cu_3(PO_4)_2$ as an anion container for ADIB (Yu et al., 2021). And, Kim et al. introduced an aqueous dual-ion system based on Mg-Cl superhalides as charge carriers in graphite cathode (Kim et al., 2020).

Until recently, Deng et al. reported a new type of dual-ion asymmetric supercapacitor based on Nb_2O_5 anode and $Ni(OH)_2$ cathode reaction with Li^+ and OH^-, respectively, and Li et al. introduced an aqueous dual-ion hybrid supercapacitor based on $NiCo_2O_4$ cathode in LiOH electrolyte (Deng et al., 2019; Li et al., 2016a, 2016b). Similarly, we developed a dual-ion system by employing cation-rich Mn-Cu oxides heterostructures cathode as anion host with lower working potentials (Jiang et al., 2021).

Nevertheless, as for above mentioned dual-ions supercapacitor or battery based on dual-ions working mechanism, wherein the cathode materials usually as the anion-storing host rather than anode (Figure 1). In order to extend the range of anion-storing materials, recent effort was made to develop new anode materials as anion hosting, where polymers, $Zn_3[Fe(CN)_6]_2$, metal-organic frameworks, etc. have been demonstrated to be capable of hosting anions at lower potentials in high-concentrated aqueous/nonaqueous electrolytes (Wu et al., 2019a, 2019b; Zhang et al., 2018a, 2018b; Dou et al., 2021). Nonetheless, it remains challenging to design new anode materials as anion hosting in dilute aqueous electrolytes. Vanadium nitride (VN) is a promising anion-storage material due to its wide operation potential (0 V to −1.2 V) and high specific capacitance (Liu et al., 2020).

Herein, we designed a high-performance VN anode as anion storage host in dilute alkali electrolytes. Benefitting from the merits of integrated electrodes and continuous multidimensional porous structure, it ensures effective ion access to the electrochemically active materials without limiting charge transport.

[1]Guangxi Key Laboratory of Electrochemical and Magneto-chemical Functional Materials, College of Chemistry and Biological Engineering, Guilin University of Technology, Guilin 541004, China

[2]Guangdong Institute of Semiconductor Industrial Technology, Guangdong Academy of Science, Guangzhou 510650, China

[3]Lead contact

*Correspondence: btliu2018@glut.edu.cn

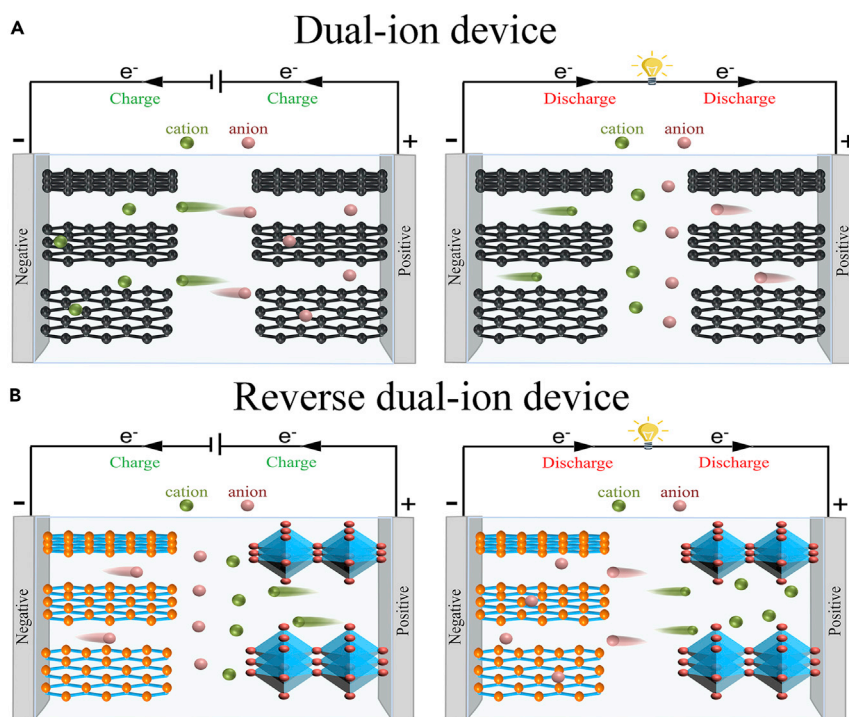https://doi.org/10.1016/j.isci.2022.104141

Figure 1. Schematic illustrations of the charge/discharge processes
(A) Conventional dual-ion device.
(B) Reverse dual-ion device.

Such a MPs VN anode exhibited exciting charge-transfer resistance (0.05 Ω), and high specific capacitance of 251 mF cm^{-2} at high scan rate. To further demonstrate the excellent performance, we further develop a reverse dual-ion hybrid supercapacitor (RDHSC) that employs MPs VN as the anode and $K_{2-x}Mn_8O_{16}$ NSs/CC as the cathode. The RDHSC exhibits a satisfactory high areal capacitance (291.7 mF cm^{-2}) and high energy density (156.3 μWh cm^{-2}). Meanwhile, the RDHSC achieves an excellent high-rate performance and cycling stability (92.2% after 10,000 cycles at 100 mV s^{-1}). Our RDHSC may open up a new route for the design of high-performance supercapacitors.

RESULTS

Structure characterizations and electrochemical properties of MPs VN electrodes

The MPs VN were designed as anion-storage materials to enhance electrode charge storage ability, and prepared by a sample annealing thermal-assisted anodizing method combined. Owning to vanadium oxide film tends to dissolve as vanadyl ions in the aqueous solution during anodizing process (Yang et al., 2011). To induce the porous structure, the $Na_2B_4O_7$ as extra oxygen source is introduced in the solution (Lewis and Perkins, 1979). The nanoporous (NPs) V_2O_5 electrodes were prepared by anodizing process. Representative scanning electron microscopy (SEM) images (Figure S1) show that $Na_2B_4O_7$ or H_2O is used as an oxygen source for vanadium oxide layer, from which it can be seen that used H_2O as an oxygen source leads to the corrosion and dissolution of vanadium oxide NPs layer (Figure S1B). While, used $Na_2B_4O_7$ as an oxygen source to grow uniform distribution NPs vanadium oxide films (Figures S1A and S5) that consists of NPs with diameter sizes distribution from ∼60 to ∼100 nm, which is consistent with pore size distribution (PSD) plots. Compared with the primary-vanadium foil, the X-ray diffraction (XRD) patterns for vanadium foil after annealing were shown in Figure 3A. The characteristic peak of pre-treated sample at 2θ = 42° can be corresponded to the orthorhombic phase V_2O_5 (JCPDS No. 41-1426), suggesting that the metal V transformed to the V_2O_5 during anodizing process. Then, the numerous mesoporous formed by following annealing in an NH_3 environment because oxygen atom replaced nitrogen atom (Chen et al., 2020), as confirmed by HR-TEM and corresponding elemental mapping of the MPs VN sample shown in Figures 2D and 2E. Compared with NPs V_2O_5 electrode, the VN electrode was induced to produce
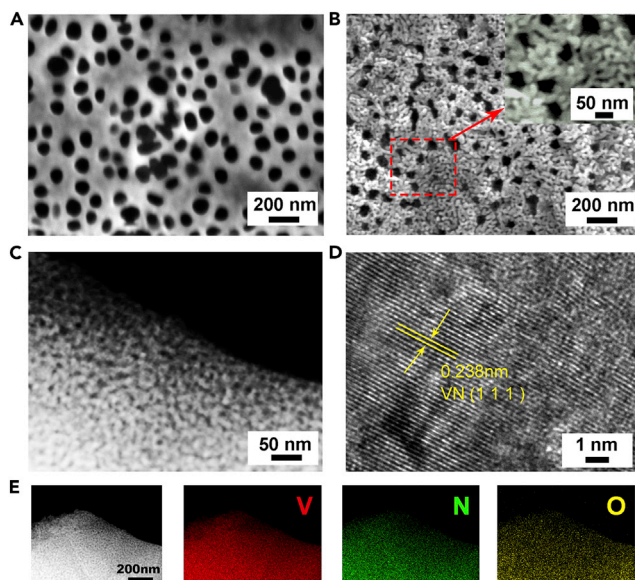
Figure 2. Microstructural characterizations of MPs VN samples

(A) Top-view SEM images of NPs V_2O_5 samples.

(B) Top-view low/high (inset)-magnification SEM images of MPs VN samples.

(C) TEM images of MPs VN samples.

(D) HR-TEM images of MPs VN samples.

(E) HR-TEM images and corresponding elemental mapping images of the MPs VN samples.

numerous mesoporous with size distribution from ~2 to ~10 nm (Figures 2B and S5). It is noteworthy that the MPs VN electrode could further increase the active material-electrolyte contact area and enhance ion diffusion/electron transport, which is very critical to improving electrochemical performance (Wang et al., 2015; Yao et al., 2020).

The phase composition and structure of MPs VN sample was determined by X-ray diffraction (XRD) pattern, high-resolution transmission electronic microscope (HR-TEM), and the corresponding element mapping images. The diffraction peaks of VN sample at 37.6°, 43.7°, 63.8°, and 80.3° correspond to VN (JCPDS No. 35-0768) phase (Figure 3A). Additionally, the HR-TEM image shows clear lattice fringe with interspacing of 0.238 nm, which is consistent with the (111) crystal planes of VN (Figure 2D). The element mapping of the VN sample (Figure 2E) shows that V, N, and O elements are homogeneously distributed, which further confirms the composition of sample.

To further determine the surface state information of the MPs VN, the X-ray photoelectron spectroscopy (XPS) spectra were performed. The full XPS spectra of MPs VN indicate that it contains of C, N, O, and V elements (Figure 3B), which is in accordance with elemental mapping (Figure 2E). The V 2p XPS spectrum shows a distinct characteristic peak at the binding energy of 513.75, 514.95, and 516.95 eV, and corresponding to V-N, V-N-O, and V-O bond, indicating the existence of V^{3+}, V^{4+}, and V^{5+} valence states (Figure 3C) (Ma et al., 2020; Ding et al., 2019). In addition, this result suggesting the presence of a partial oxidation layer on the surface of VN was caused by air (Zhang et al., 2018a, 2018b). For the N 1s spectrum, one sharp peak at 397.2 eV, corresponding to N-V bonding, and other peaks at 399.1 eV attributed to V-N-O asymmetric stretching mode (Figure 3D) (Zhao et al., 2016). These results support that surfaced V_2O_5 are converted into VN through nitridation treatment, and forming mesoporous structure.

To investigate the electrochemical behavior on the MPs VN electrode, the cyclic voltammetry (CV) curves, galvanostatic charge-discharge (GCD) profiles and electrochemical impedance spectroscopy (EIS) were examined in 1 M KOH electrolyte. The CV curves of MPs VN electrode from −1.3 V to 0 V (vs. Ag/AgCl) at 50 mV s^{-1} were shown in Figure 4A. It is worth noting that the CV curve exhibits two pairs of symmetric redox peaks, the anodic peaks are at −0.64 V and −0.97 V and relevant cathodic peaks at −0.76 V and −1.1 V, indicating the reversible redox occurs on MPs VN electrode surface. Specifically, the reaction
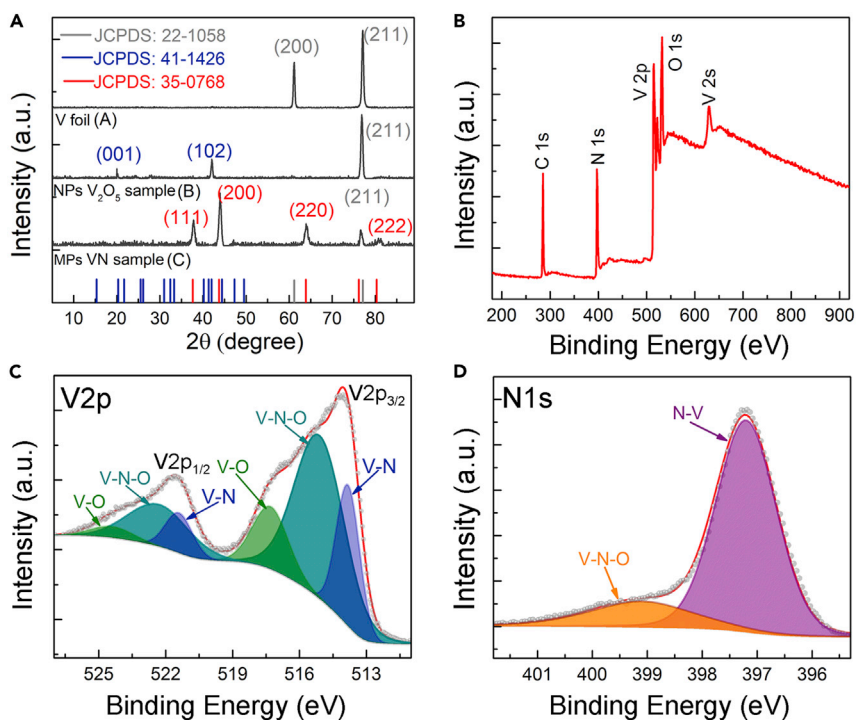
Figure 3. Chemical analysis and electrical properties of MPs VN samples
(A) XRD patterns of vanadium foil (A curve), NPs V_2O_5 (B curve) and MPs VN samples (C curve).
(B) XPS survey spectrum of the MPs VN samples.
(C) High-resolution XPS spectra of V 2p for VN samples.
(D) High-resolution XPS spectra of N 1s for VN samples.

mechanism of the VN arises from a combination of an electrical double-layer formation and the faradic redox reactions that occur on the surface of these partially oxidized nitrides (Choi et al., 2006). Owing to the presence of OH^- ions, it could lead to the occurrence of an equilibrium reaction at high pH, such as the one shown below on the surface of the nitride (or oxynitride) electrode:

$$2V^{3+}N_xO_y + 2OH^- + e^- \leftrightarrow V^{3+}N_xO_y \parallel OH^- + V^{2+}N_xO_yOH$$
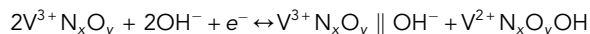
where $VN_xO_y\parallel OH^-$ represents electrical double layer formed by the hydroxyl ions adsorbed on the oxynitride surface induced by ion-dipole attraction which leads to a substantial increase in the specific capacitance (according to most widely accepted theory). Notably, some recent studies on the reaction mechanism of vanadium nitride have shown other possibilities (Liu et al., 2021; Yang et al., 2022).

Sweep voltammetry also provides greater insight into the difference in charge storage kinetics of the MPs VN electrodes. According to previous report, the cathodic/anodic peak current (i) and the scan rate (v) can follow the relationship:

$$\log(i) = a\log(v) + \log(b)$$

where a and b are adjustable parameters. When a-value approaches 0.5, the electro-chemical system is mainly controlled by ionic diffusion, but when the a-value is close to 1, the pseudocapacitive effect dominates (Jiang and Liu, 2019; Wu et al., 2019a, 2019b). Figure 4B displays the plots of $\log(i)$ vs. $\log(v)$ at the two cathodic/anodic peak pair, where the a-value for the anodic (I, II) and cathodic (III, IV) reactions are determined to be 0.882, 0.962, 0.815, and 0.943, respectively, indicating the electrochemical system is mainly controlled by the pseudocapacitive. The pseudocapacitive contributions at various scan rates could be calculated from the equation:
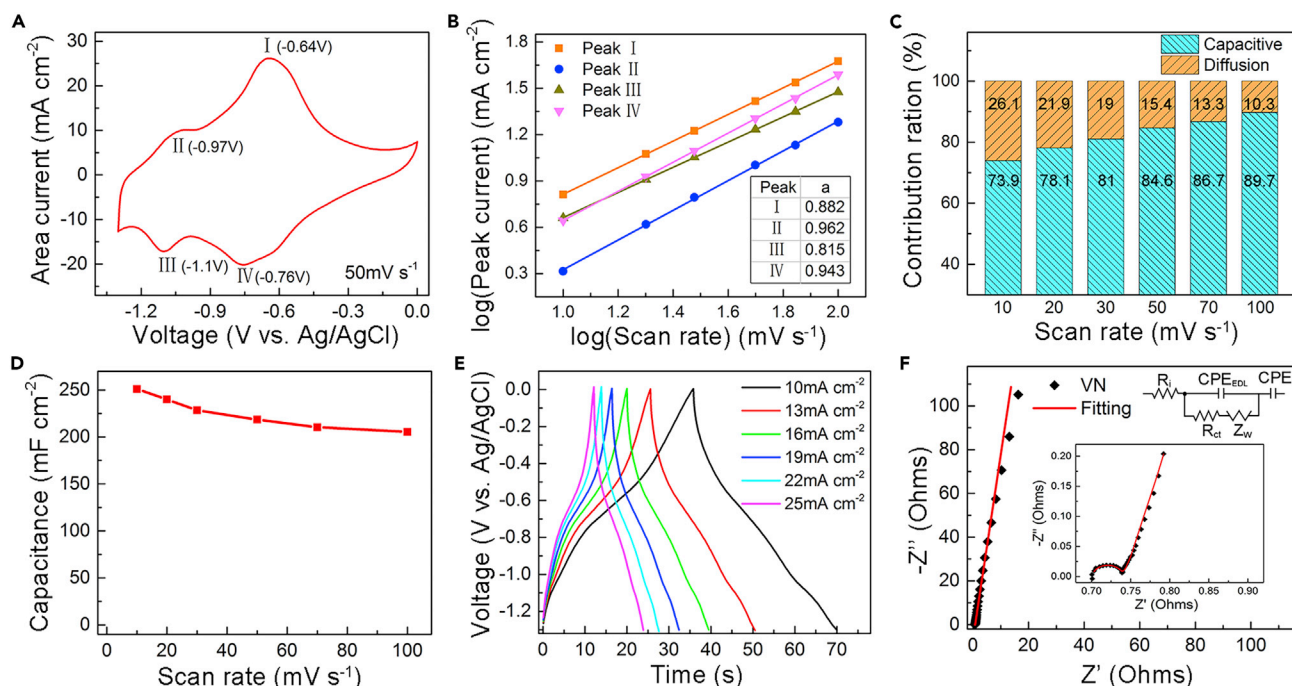
$$i(V) = k_1 v + k_2 v^{1/2}$$

Figure 4. Electrochemical characterizations of MPs VN electrodes with a three-electrode system

(A) CV curve of MPs VN electrodes at 50 mV s^{-1} in 1 M KOH electrolyte.

(B) Plots of log (I) vs. log(v) at cathodic/anodic peaks (peak current: i; scan rate: v).

(C) Percentages of pseudocapacitive contributions to charge storage in MPs VN electrodes at scan rates from 10 to 100 mV s^{-1}.

(D) Areal capacitance of the MPs VN electrodes as a function of various scan rates (10–100 mV s^{-1}).

(E) GCD profiles of MPs VN electrodes at various current densities from 10 to 25 mA cm^{-2}.

(F) EIS spectras of MPs VN electrodes (Inset show equivalent circuit for EIS data fitting).

where $k_1 v$ and $k_2 v^{1/2}$ represent the contribution of pseudocapacitive effect and ionic diffusion, respectively (Wang et al., 2016a, 2016b). As shown in Figures 4C and S2B, the pseudocapacitive contributions 73.9%, 78.1%, 81.2%, 84.6%, 86.7%, and 89.7% of the total capacity at 10 mV s^{-1}, 20 mV s^{-1}, 30 mV s^{-1}, 50 mV s^{-1}, 70 mV s^{-1}, and 100 mV s^{-1}, respectively.

As demonstrated in Figure S2A, the CV curves of the MPs VN electrode are at various scan rates. Two pairs of redox peaks are located at ∼ -0.65/∼-0.75 V and ∼-0.95/∼-1.1V in CV curves. With the increasing scan rate, the curves maintain similar shape and increase the current density of characteristic peaks; at the same time, the reduction and oxidation peaks only slightly shift toward higher and lower potentials, respectively. Benefitting from mesoporous and high conductivity, the MPs VN electrode could achieve satisfactory charge storage ability (Djire et al., 2019). At 10 mV s^{-1}, the MPs VN electrode displays an area capacitance of ∼251 mF cm^{-2} (Figure 4D). Even when the scan rate is increased to 100 mV s^{-1}, the MPs VN electrode still retains a capacitance of ∼205.4 mF cm^{-2} (∼81.9%), indicating its excellent capacitive behavior and high-rate charging capability. Additionally, the GCD profiles (Figure 4E) exhibit a near-perfect isosceles triangle without obvious IR-drop behavior at various current densities. The results of MPs VN electrode suggest its high electrical conductivity and excellent electrochemical reversibility. In addition, the EIS was further utilized to support the above analysis (Figure 4F). In general, the impedance spectrum including intercept at the real axis in high frequency, semicircles at high to medium-frequency ranges, and one oblique line in the low frequency region are related to the internal resistance of the electrodes and the Ohmic resistance of electrolyte, charge-transfer resistance, and ion transfer resistance, respectively. It was found that the internal resistance (R_i, 0.7Ω) and charge-transfer resistance (R_{ct}, 0.05 Ω) is much very small, which is consistent with IR-drop results in GCD profiles. These results imply that MPs VN electrode possess fast charge transfer and ion diffusion kinetics in case of high rates. Such outstanding electrochemical properties are attributed to vanadium nitride with good electrical conductivity and mesoporous structure.
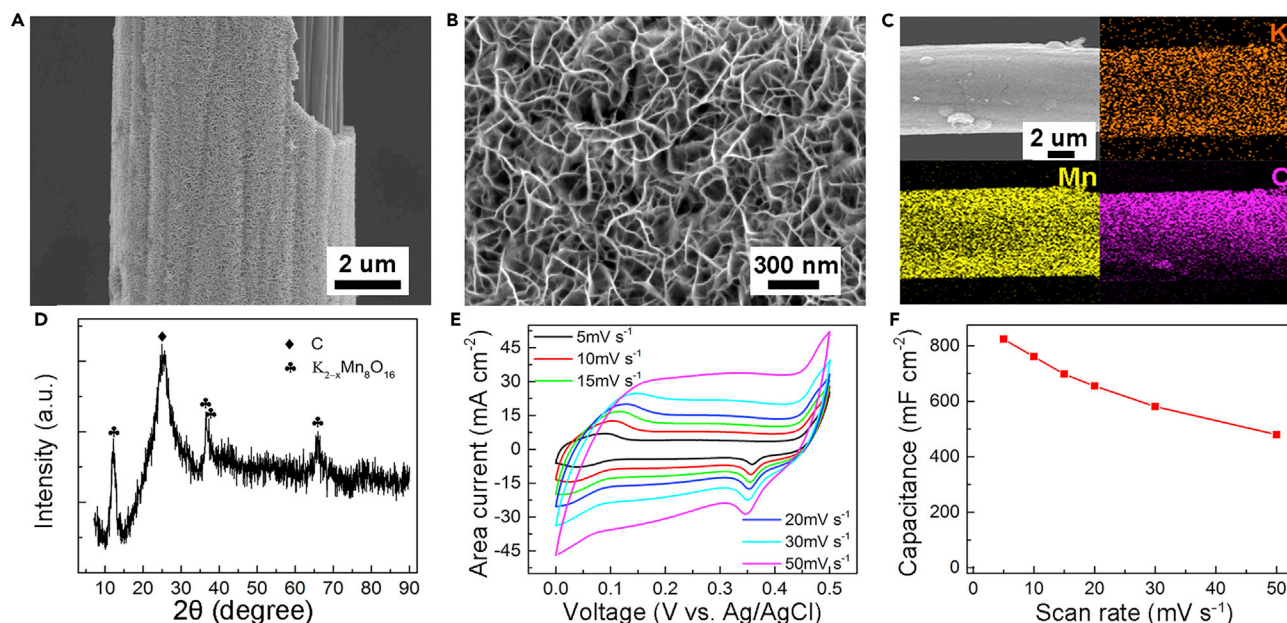
Figure 5. Microstructural and electrochemical characterizations of K$_{2-x}$Mn$_8$O$_{16}$ NSs/CC electrodes with a three-electrode system
(A) Typical low-magnification SEM images of K$_{2-x}$Mn$_8$O$_{16}$ NSs/CC electrode.
(B) Typical high-magnification SEM images of K$_{2-x}$Mn$_8$O$_{16}$ NSs/CC electrode.
(C) SEM images of the K$_{2-x}$Mn$_8$O$_{16}$ NSs/CC electrode and corresponding elements mapping images of K, Mn, and O.
(D) XRD patterns of K$_{2-x}$Mn$_8$O$_{16}$ NSs/CC electrode.
(E) CV curves of K$_{2-x}$Mn$_8$O$_{16}$ NSs/CC electrode measured at different scan rates from 5 to 50 mV s^{-1}.
(F) Areal capacitance of K$_{2-x}$Mn$_8$O$_{16}$ NSs/CC electrode at various scan rates.

Structure characterizations and electrochemical properties of K$_{2-x}$Mn$_8$O$_{16}$ NSs/CC electrodes

To further evaluate its applications, a dual-ion hybrid supercapacitor was fabricated employing MPs VN electrode as anode and K$_{2-x}$Mn$_8$O$_{16}$ NSs/CC electrode as cathode. For this reason, the K$_{2-x}$Mn$_8$O$_{16}$ NSs were directly grown on the surface of carbon cloth as cathode via a simple hydrothermal method. As shown in Figure 5B, the K$_{2-x}$Mn$_8$O$_{16}$ NSs/CC exhibited a highly open and porous structure assembled from perpendicular interlaced nanosheets. Meanwhile, the low-magnification SEM image of the K$_{2-x}$Mn$_8$O$_{16}$ NSs/CC electrode is shown in Figures 5A and S6, which clearly see the electrode containing ~500 nm thick K$_{2-x}$Mn$_8$O$_{16}$ layer. Representative SEM images of K$_{2-x}$Mn$_8$O$_{16}$/nanofiber and corresponding element mappings for K, Mn, and O are shown in Figure 5C. The distribution of K, Mn, and O elements is consistent with the SEM image of K$_{2-x}$Mn$_8$O$_{16}$ NSs/CC electrode, which indicates that K and Mn are distributed uniformly in the fibers. The crystal structure of K$_{2-x}$Mn$_8$O$_{16}$ NSs/CC electrode further confirmed by XRD was shown in Figure 5D. Well-defined diffraction peaks at 2θ valves of 12.7°, 36.7°, 37.7°, and 65°, correspond to (1 1 0), (4 0 0), (2 1 1), and (0 2 0) diffraction planes of K$_{2-x}$Mn$_8$O$_{16}$ (JCPDS No. 44-1386).

The electrochemical properties of the K$_{2-x}$Mn$_8$O$_{16}$ NSs/CC electrodes were evaluated by the CV curves, GCD profiles, and EIS spectra; these curves are carried out at a potential sweep window ranging from 0 to 0.5 V. The reaction equation in the electrochemical charge and discharge process can be expressed by the following equations:

$$MnO_2 + H_3O^+ + xK^+ + (x+1)e^- \leftrightarrow K_xMnOOH + OH^-$$
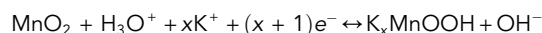
The charge storage mechanism of cathode material involves a redox reaction through both potassium ion exchange and proton exchange (Wang et al., 2016a, 2016b). Detail electrochemical behavior of the K$_{2-x}$Mn$_8$O$_{16}$ NSs/CC electrode was analyzed by typical CV curves at different scan rates, as shown in Figure 5E. The K$_{2-x}$Mn$_8$O$_{16}$ NSs/CC electrode displays an area capacitance of as high as 824 mF cm^{-2} at a scan rate of 5 mV s^{-1} (Figure 5F). Such a high pseudocapacitive charge storage capacity for

$K_{2-x}Mn_8O_{16}$ NSs/CC electrode is achieved through pre-inserted K^+ ions (Jabeen et al., 2016; Karikalan et al., 2017). The typical redox peak of CV curve can be attributed to the intercalation/de-intercalation of hydrated K^+ from the electrolyte into the MnO_2 (Zhang et al., 2020; Liu et al., 2019). Even when increasing scan rate to 50 mV s^{-1}, it still retains a capacitance of 480 mF cm^{-2}, implying its excellent rate capability. Figure S3A shows the GCD profiles of the $K_{2-x}Mn_8O_{16}$ NSs/CC electrode at various current densities, where the voltage plateaus are observed between ∼0.5 and ∼0.45 V is consistent with CV results. The GCD profiles showing triangular shapes without obvious IR-drop behavior was observed. In addition, the EIS measurements were conducted for further examining the performance of $K_{2-x}Mn_8O_{16}$ NSs/CC electrodes. The Nyquist plots of the $K_{2-x}Mn_8O_{16}$ NSs/CC electrodes are shown in Figure S3B. The internal resistance (1.2Ω) and charge transfer resistance (2.6Ω) are very small, which is consistent with IR-drop result.

Electrochemical behavior of RDHSC devices

To further demonstrate its practical applications, the reverse dual-ion supercapacitor fabricated by using MPs VN anode (within the potential range of −1.3 to 0 V) and $K_{2-x}Mn_8O_{16}$ NSs/CC cathode (within the potential range of 0–0.5 V). Therefore, the comparative CV curves of $K_{2-x}Mn_8O_{16}$ NSs/CC cathode and MPs VN anode were shown in Figure 6A (at 50 mV s^{-1}). It should be noted that the mass ratio of MPs VN anode to $K_{2-x}Mn_8O_{16}$ NSs/CC cathode was accomplished by controlling the deposition mass of $K_{2-x}Mn_8O_{16}$ (based on charge balance between the cathode and anode). Figure 6B shows the representative CV curves of the RDHSC at scan rates ranging from 5 to 100 mV s^{-1} within a voltage window of 0–1.8 V. Obviously, the redox peaks can be clearly observed in all CV curves, indicating the typical battery-type electrochemical behavior of RDHSC. Meanwhile, the elemental analysis results of the original and charge-discharge-activated $K_{2-x}Mn_8O_{16}$ cathodes were characterized by inductively coupled plasma (ICP). The ICP results show that the K/Mn ratio at the end of discharging increased from 8.8 to 20.6, which imply the insertion of K ions during discharging, and further demonstrate work mechanism of the DHSC devices (Table S1).With the increasing of scan rate, it can be seen that the redox current increases accordingly and the shape of the CV curves is not obviously changed, suggesting ideal charge storage behavior and desirable rapid charge/discharge property of our device (Mohanty et al., 2021). As shown in Figure 6D, it achieved a high capacitance of 291.7 mF cm^{-2} at 5 mV s^{-1}, which enlists RDHSC beyond the most reported thin film devices. Even when increasing the scan rate to 100 mV s^{-1}, it still retains the capacity of 164 mF cm^{-2}, which is about 1.5–10 times higher than that of the thin film hybrid devices (Figure S4B). These detailed information includes: e-WO$_3$//MnO$_2$ (14.3 mF cm^{-2} at 20 mV s^{-1}), GCF11//GMF9 (33.6 mF cm^{-2} at 10 mV s^{-1}), MoSe$_2$@CN//MoSe$_2$@CN (70.2 mF cm^{-2} at 5 mV s^{-1}), CNT@MnO$_2$//CNT@PPy (60.5 mF cm^{-2} at 10 mV s^{-1}), Fe$_2$O$_3$//NiO@MnO$_2$ (48.1 mF cm^{-2} at 1 mV s^{-1}, 28 mF cm^{-2} at 100 mV s^{-1}), CNT//CNT@ZnO-NWs@MnO$_2$ (30.1 mF cm^{-2} at 5 mV s^{-1}, 18.3 mF cm^{-2} at 50 mV s^{-1}), and CNT@CNF//CNF (87 mF cm^{-2} at 2 mV s^{-1}) (Zhu et al., 2015; Zheng et al., 2014; Ojha and Deepa, 2019; Yu et al., 2017; Liu et al., 2018; Li et al., 2016a, 2016b; Le et al., 2013). These above results prove its excellent rate performance and charge storage ability. It agrees well with the GCD profiles, where the shape resembling an isosceles triangle without an obviously IR-drop at various current densities ranging from 5 to 15 mA cm^{-2}, as shown in Figure 6C. To further evaluate its electrochemical behavior, the EIS spectrum was performed in a frequency range of 10^{-2} to 10^5 Hz, as shown in Figure 6E. The EIS data were fit by an equivalent circuit model of the RDHSC as shown in the inset of Figure S4A. Here, the internal resistance of our RDHSC was as low as 0.97 Ω and charge transfer resistance was 2.1 Ω, and the inclination of nearly 90° in Nyquist plot indicated idea capacitive behavior. Meanwhile, the cycling stability of RDHSC was further investigated by CV curves at scan rate of 100 mV s^{-1} in Figure 6G. Our RDHSC devices exhibit an excellent reversibility and high capacity retention of 92.2% after 10,000 cycles.

The energy density and power density are critical factors for its practical application. In the Ragone plots, Figure 6F compares the areal performance of our RDHSC to those of previously reported hybrid supercapacitors. The RDHSC devices exhibit a maximum energy density of 156.3 μWh cm^{-2} (based on two electrodes) at the power density of 0.94 mW cm^{-2}. Even at a high power density of 14.76 mW cm^{-2}, the energy density can still retain 73.8 μWh cm^{-2}. These values are substantially much higher than those recently reported hybrid supercapacitors, including P-TiON//VN (32.4 μWh cm^{-2} at 0.9 mW cm^{-2}), CWS/Ni//grapheme (102 μWh cm^{-2} at 0.675 mW cm^{-2}, 7.5 μWh cm^{-2} at 27 mW cm^{-2}), MnO$_2$/PEDTO//VN/C NWAs/CNT (96 μWh cm^{-2} at 0.27 mW cm^{-2}, 52 μWh cm^{-2} at 2.7 mW cm^{-2}), RuO$_2$//VN (20 μWh cm^{-2} at 3 mW cm^{-2}), LiCoO$_2$//Fe$_2$O$_3$/FeOOH (56.25 μWh cm^{-2} at 1.1 mW cm^{-2}), PNC/PEDTO//CMK (11 μWh cm^{-2} at 0.33 mW cm^{-2}, 6.1 μWh cm^{-2} at
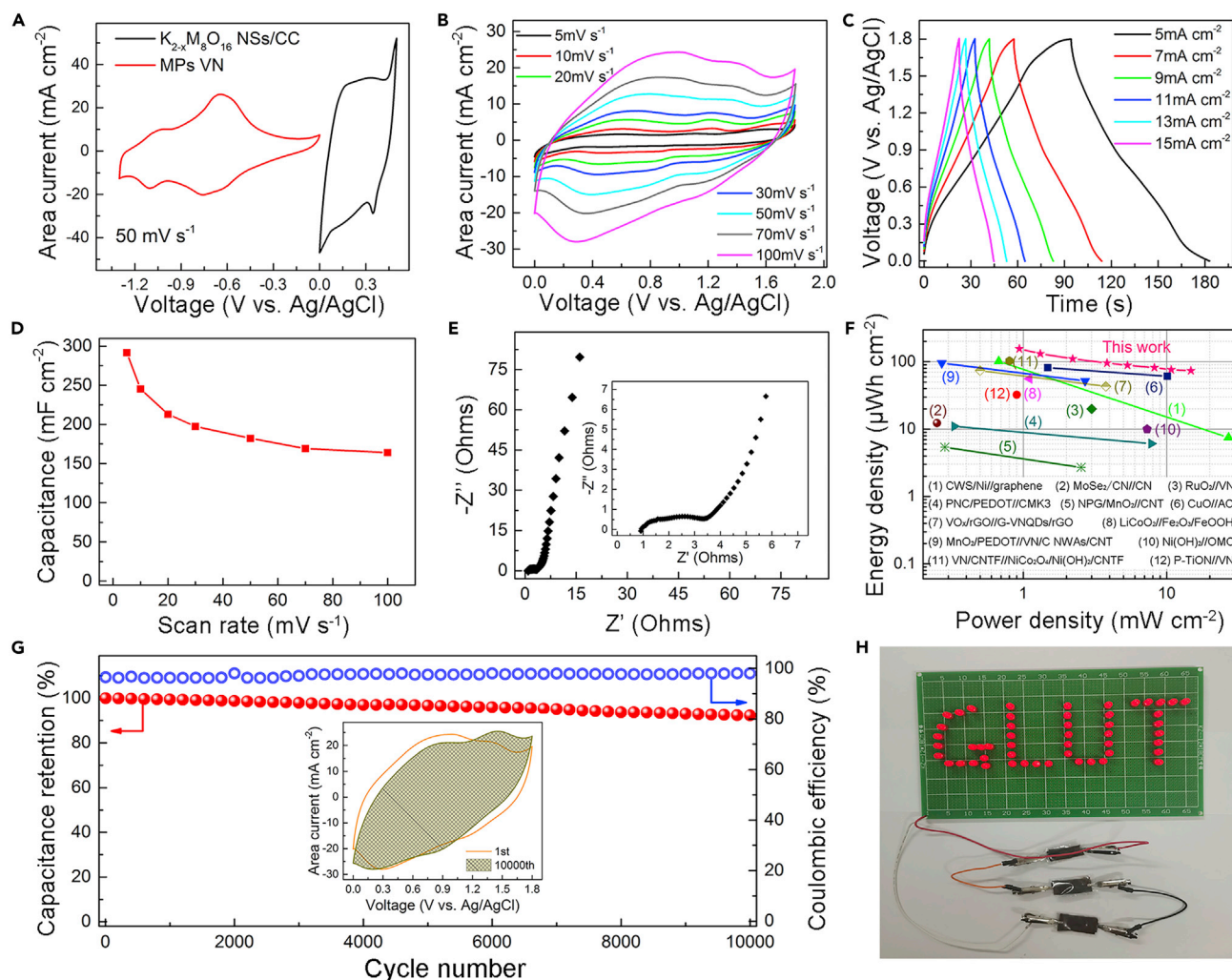
Figure 6. Electrochemical behavior of RDHSC devices

(A) CV curves of MPs VN electrode and $K_{2-x}Mn_8O_{16}$ NSs/CC electrode at 50 mV s^{-1}, respectively.

(B) CV curves of RDHSC at various scan rates.

(C) GCD profiles of RDHSC at different current densities from 5 to 15 mA cm^{-2}.

(D) Areal capacitance of the RDHSC as a function of various scan rates.

(E) EIS spectra of RDHSC.

(F) Ragone plot comparing stack energy and power densities of RDHSC with other thin film devices.

(G) Cycling performance and coulombic efficiency of the RDHSC devices at a scan rate of 100 mV s^{-1}, inset are CV curves of first and 10000th.

(H) Photographs of the three RDHSC devices in series powering an LED array containing 50 bulbs.

7.8 mW cm^{-2}), VN/CNTF//NiCo$_2$O$_4$/Ni(OH)$_2$/CNTF (103.8 μWh cm^{-2} at 0.8 mW cm^{-2}), CuO//AC (82 μWh cm^{-2} at 1.48 mW cm^{-2}, 61 μWh cm^{-2} at 10.1 mW cm^{-2}), Ni(OH)$_2$//OMC (10 μWh cm^{-2} at 7.3 mW cm^{-2}), MoSe$_2$/CN//CN (12.3 μWh cm^{-2} at 0.25 mW cm^{-2}), NPG/MnO$_2$//CNT (5.4 μWh cm^{-2} at 0.284 mW cm^{-2}, 2.7 μWh cm^{-2} at 2.53 mW cm^{-2}), and VO$_x$/rGO//G-VNQDs/rGO (73.9 μWh cm^{-2} at 0.5 mW cm^{-2}, 43.1 μWh cm^{-2} at 3.77 mW cm^{-2}) (Yang et al., 2016, 2020; Pazhamalai et al., 2019; Zhang et al., 2017; Asbani et al., 2021; Lu et al., 2020; Wang et al., 2019; Cha et al., 2017; Dong et al., 2014; Ojha and Deepa, 2019; Xu et al., 2015; Shen et al., 2018). To further demonstrate its application, 50 LEDs in parallel also work well powered by these three devices (device area is 2 cm^2) in-series (Figure 6H). These outstanding comprehensive performances fully support our hypothesis that unique charging mechanism of MPs VN as anion storage electrode to realize high-performance energy storage, which makes them potentially competitive against typical hybrid supercapacitor.

DISCUSSION

In summary, we have proposed an RDHSC based on MPs VN anode as anion storage material. Compared with traditional dual-ion systems, the direction of ions movement in RDHSC is reversed, that is, OH^- and K^+ are extracted from anode and cathode during charging process, respectively. The RDHSC with a maximum operating voltage of 1.8 V, the charge transfer resistance is as low as 0.97 Ω and interfacial resistance is only 2.6 Ω. Therefore, the RDHSC exhibits a remarkable high specific capacitance of 291.7 mF cm^{-2}, its maximum energy density reaches 156.3 μWh cm^{-2} at a power density of 0.94 mW cm^{-2}, and energy density of 73.8 μWh cm^{-2} is maintained even at a high power density of 14.76 mW cm^{-2}. Moreover, the RDHSC exhibits an excellent reversibility and high capacity retention of 90% after 10,000 cycles.

Limitations of the study

This mesoporous vanadium nitride only exhibits excellent anion storage properties in alkaline medium, which limits its further wide application in devices. Therefore, in future work, we will design and prepare the anion-storage materials with wider medium adaptability while maintaining the easy processability, mechanical stability, and ideal electrochemical performance.

STAR★METHODS

Detailed methods are provided in the online version of this paper and include the following:

- KEY RESOURCES TABLE
- RESOURCE AVAILABILITY
  - Lead contact
  - Materials availability
  - Data and code availability
- METHOD DETAILS
  - Materials
  - Synthesis of MPs VN electrode
  - Synthesis of $K_{2-x}Mn_8O_{16}$ NSs/CC electrode
  - Materials characterization
  - Electrochemical measurements and calculations

SUPPLEMENTAL INFORMATION

Supplemental information can be found online at https://doi.org/10.1016/j.isci.2022.104141.

AUTHOR CONTRIBUTIONS

B.-T.L. and C.S. conceived and designed the experiments. B.-T.L., C.S., F.J., W.C., and Y.P. carried out the fabrication of materials and performed the electrochemical and microstructural characterizations. B.-T.L. and C.S. wrote the paper, and all authors discussed the results and commented on the manuscript.

DECLARATION OF INTERESTS

The authors declare no competing interests.

INCLUSION AND DIVERSITY

While citing references scientifically relevant for this work, we also actively worked to promote gender balance in our reference list.

REFERENCES

Asbani, B., Robert, K., Roussel, P., Brousse, T., and Lethien, C. (2021). Asymmetric micro-supercapacitors based on electrodeposited RuO_2 and sputtered VN films. Energy Storage Mater. *37*, 207–214.

Cha, S., Nagaraju, G., Sekhar, S., and Yu, J. (2017). A facile drop-casting approach to nanostructured copper oxide painted conductive woven textile as binder-free electrode for improved energy storage performance in redox-additive electrolyte. J. Mater. Chem. A *5*, 2224–2234.

Chen, M., Fan, H., Zhang, Y., Liang, X., Chen, Q., and Xia, X. (2020). Coupling PEDOT on mesoporous vanadium nitride arrays for advanced flexible all-solid-state supercapacitors. Small *16*, 2003434.

Choi, B.D., Blomgren, G., and Kumta, P. (2006). Fast and reversible surface redox reaction in nanocrystalline vanadium nitride supercapacitors. Adv. Mater. *18*, 1178–1182.

Deng, X., Jiang, Y., Wei, Z., Mao, M., Pothu, R., Wang, H., Wang, C., Liu, J., and Ma, J. (2019). Flexible quasi-solid-state dual-ion asymmetric supercapacitor based on $Ni(OH)_2$ and Nb_2O_5 nanosheet arrays. Green Energy Environ. *4*, 382–390.

Ding, J., Du, Z., Li, B., Wang, L., Wang, S., Gong, Y., and Yang, S. (2019). Unlocking the potential of disordered rocksalts for aqueous zinc-ion batteries. Adv. Mater. *31*, 1904369.

Djire, A., Pande, P., Deb, A., Siegel, J., Ajenifujah, O., He, L., Sleightholme, A., Rasmussen, P., and Thompson, L. (2019). Unveiling the pseudocapacitive charge storage mechanisms of nanostructured vanadium nitrides using in-situ analyses. Nano Energy *60*, 72–81.

Dong, X., Guo, Z., Song, Y., Huo, M., Wang, J., Wang, Y., and Xia, Y. (2014). Flexible and wire-shaped micro-supercapacitor based on $Ni(OH)_2$-nanowire and ordered mesoporous carbon electrodes. Adv. Funct. Mater. *24*, 3405–3412.

Dou, Q., Wu, N., Yuan, H., Shin, K.H., Tang, Y., Mitlin, D., and Park, H.S. (2021). Emerging trends in anion storage materials for the capacitive and hybrid energy storage and beyond. Chem. Soc. Rev. *50*, 6734–6789.

Dunn, B., Kamath, H., and Tarascon, J. (2011). Electrical energy storage for the grid: a battery of choices. Science *334*, 928–935.

Jabeen, N., Xia, Q., Savilov, S., Aldoshin, S., Yu, Y., and Xia, H. (2016). Enhanced pseudocapacitive performance of α-MnO_2 by cation preinsertion. ACS Appl. Mater. Interfaces *8*, 33732–33740.

Jiang, Y., and Liu, J. (2019). Definitions of pseudocapacitive materials: a brief review. Energy Environ. Mater. *2*, 30–37.

Jiang, L., Shi, C., Pang, Y., Liu, Y., Li, J., Mai, W., and Liu, B.T. (2021). Semi-coherent cation-rich Mn-Cu oxides heterostructures as cathode for novel aqueous potassium dual-ion energy storage devices. J. Colloid Interface Sci. *597*, 75–83.

Karikalan, N., Karuppiah, C., Chen, S., Velmurugan, M., and Gnanaprakasam, P. (2017). Three dimensional fibrous network of $Na_{0.21}MnO_2$ for aqueous sodium ion hybrid supercapacitor. Chem. Eur. J. *23*, 2379–2386.

Kim, K., Guo, Q., Tang, L., Zhu, L., Pan, C., Chang, C., Razink, J., Lerner, M., Fang, C., and Ji, X. (2020). Reversible insertion of Mg-Cl superhalides in graphite as a cathode for aqueous dual-ion battery. Angew. Chem. Int. Ed. *132*, 20096–20100.

Larcher, D., and Tarascon, J. (2015). Towards greener and more sustainable batteries for electrical energy storage. Nat. Chem. *7*, 19–29.

Le, V., Kim, H., Ghosh, A., Kim, J., Chang, J., Vu, Q., Pham, D., Lee, J., Kim, S., and Lee, Y. (2013). Coaxial fiber supercapacitor using all-carbon material electrodes. ACS Nano *7*, 5940–5947.

Lewis, M.B., and Perkins, R.A. (1979). The source of oxygen in the anodization of vanadium. J. Electrochem. Soc. *126*, 544–547.

Li, Y., Tang, F., Wang, R., Wang, C., and Liu, J. (2016a). Novel dual-ion hybrid supercapacitor based on a $NiCo_2O_4$ nanowire cathode and MoO_2−C nanofilm anode. ACS Appl. Mater. Interfaces *8*, 30232–30238.

Li, Y., Yan, X., Zheng, X., Si, H., Li, M., Liu, Y., Sun, Y., Jiang, Y., and Zhang, Y. (2016b). Fiber-shaped asymmetric supercapacitors with ultrahigh energy density for flexible/wearable energy storage. J. Mater. Chem. A *4*, 17704–17710.

Liu, X., Wang, J., and Yang, G. (2018). Amorphous nickel oxide and crystalline manganese oxide nanocomposite electrode for transparent and flexible supercapacitor. Chem. Eng. J. *347*, 101–110.

Liu, G., Kang, C., Fang, J., Fu, L., Zhou, H., and Liu, Q. (2019). MnO_2 nanosheet-coated Co_3O_4 complex for 1.4 V extra-high voltage supercapacitors electrode material. J. Power Sources *431*, 48–54.

Liu, Y., Wu, Q., Liu, L., Manasa, P., Kang, L., and Ran, F. (2020). Vanadium nitride for aqueous supercapacitors: a topic review. J. Mater. Chem. A *8*, 8218–8233.

Liu, Y., Liu, L., Kang, L., and Ran, F. (2021). Energy storage mechanism of vanadium nitride via intercalating different atomic radius for expanding interplanar spacing. Energy Environ. Mater. *0*, 1–7.

Lu, J., Hao, R., Li, J., Wan, J., Wang, C., Ji, P., Wang, X., Liu, G., and Hu, C. (2020). A fast composite-hydroxide-mediated approach for synthesis of 2D-$LiCoO_2$ for high performance asymmetric supercapacitor. Electrochim. Acta *331*, 135426.

Ma, M., Shi, Z., Li, Y., Yang, Y., Zhang, Y., Wu, Y., Zhao, H., and Xie, E. (2020). High-performance 3 V "water in salt" aqueous asymmetric supercapacitors based on VN nanowires electrode. J. Mater. Chem. A *8*, 4827–4835.

Meng, W., and Tang, Y. (2018). A review on the features and progress of dual-ion batteries. Adv. Energy Mater. *8*, 1703320.

Mohanty, A., Jaihindh, D., Fu, Y., Senanayak, S.P., Mende, L.S., and Ramadoss, A. (2021). An extensive review on three dimension architectural metal-organic frameworks towards supercapacitor application. J. Power Sources *488*, 229444.

Muzaffar, A., Ahamed, M., Deshmukh, K., and Thirumalai, J. (2019). A review on recent advances in hybrid supercapacitors: design, fabrication and applications. Renew. Sustain. Energy Rev. *101*, 123–145.

Ojha, M., and Deepa, M. (2019). Molybdenum selenide nanotubes decorated carbon net for a high performance supercapacitor. Chem. Eng. J. *368*, 772–783.

Pazhamalai, P., Krishnamoorthy, K., Sahoo, S., Mariappan, V., and Kim, S. (2019). Copper tungsten sulfide anchored on Ni-foam as a high-performance binder free negative electrode for asymmetric supercapacitor. Chem. Eng. J. *359*, 409–418.

Saikia, B., Benoy, S.M., Bora, M., Tamuly, J., Pandey, M., and Bhattacharya, D. (2020). A brief review on supercapacitor energy storage devices and utilization of natural carbon resources as their electrode materials. Fuel *282*, 118796.

Shao, Y., El-kady, M., Sun, J., Li, Y., Zhang, Q., Zhu, M., Wang, H., Dunn, B., and Kaner, R. (2018). Design and mechanisms of asymmetric supercapacitors. Chem. Rev. *118*, 9233–9280.

Shen, K., Ding, J., and Yang, S. (2018). 3D Printing quasi-solid-state asymmetric micro-supercapacitors with ultrahigh areal energy density. Adv. Energy Mater. *8*, 1800408.

Wang, G., Zhang, L., and Zhang, J. (2012). A review of electrode materials for electrochemical supercapacitors. Chem. Soc. Rev. *41*, 797–828.

Wang, R., Lang, J., Zhang, P., Lin, Z., and Yan, X. (2015). Fast and large lithium storage in 3D porous VN nanowires–graphene composite as a superior anode toward high-performance hybrid supercapacitors. Adv. Funct. Mater. *25*, 2270–2278.

Wang, B., Qin, J., Feng, H., Wang, N., Sakai, E., and Komiyama, T. (2016a). Preparation of MnO_2/

carbon nanowires composites for supercapacitors. Electrochim. Acta 212, 710–721.

Wang, J., Tang, H., Zhang, L., Ren, H., Yu, R., Jin, Q., Qi, J., Mao, D., Yang, M., Wang, Y., et al. (2016b). Multi-shelled metal oxides prepared via an anion-adsorption mechanism for lithium-ion batteries. Nat. Energy 1, 16050.

Wang, X., Sun, J., Zhou, J., Zhou, Z., Zhang, Q., Wong, C., and Yao, Y. (2019). All-solid-state fiber-shaped asymmetric supercapacitors with ultrahigh energy density based on porous vanadium nitride nanowires and ultrathin Ni(OH)$_2$ nanosheet wrapped NiCo$_2$O$_4$ nanowires arrays electrode. J. Phys. Chem. C 123, 985–993.

Wu, H., Yu, Q., Lao, C., Qin, M., Wang, W., Liu, Z., Man, C., Wang, L., Jia, B., and Qu, X. (2019a). Scalable synthesis of VN quantum dots encapsulated in ultralarge pillared N-doped mesoporous carbon microsheets for superior potassium storage. Energy Storage Mater. 18, 43–50.

Wu, X., Xu, Y., Zhang, C., Leonard, D., Markir, A., Lu, J., and Ji, X. (2019b). Reverse dual-ion battery via a ZnCl$_2$ water-in-salt electrolyte. J. Am. Chem. Soc. 141, 6338–6344.

Xu, H., Hu, X., Sun, Y., Yang, H., Liu, X., and Huang, Y. (2015). Flexible fiber-shaped supercapacitors based on hierarchically nanostructured composite electrodes. Nano Res. 8, 1148–1158.

Yang, Y., Albu, S., Kim, D., and Schmuki, P. (2011). Enabling the anodic growth of highly ordered V$_2$O$_5$ nanoporous/nanotubular structures. Angew. Chem. Int. Ed. 50, 9071–9075.

Yang, H., Xu, H., Li, M., Zhang, L., Huang, Y., and Hu, X. (2016). Assembly of NiO/Ni(OH)$_2$/PEDOT nanocomposites on contra wires for fiber-shaped

flexible asymmetric supercapacitors. ACS Appl. Mater. Interfaces 8, 1774–1779.

Yang, W., Zhu, Y., Jia, Z., He, L., Xu, L., Meng, J., Tahir, M., Zhou, Z., Wang, X., and Mai, L. (2020). Interwoven nanowire based on-chip asymmetric microsupercapacitor with high integrability, areal energy, and power density. Adv. Energy Mater. 10, 2001873.

Yang, Y., Wang, Y., Zhao, L., Liu, Y., and Ran, F. (2022). Visualizing nucleation and growth process of vanadiumsupramolecular nanoribbons self-assembled by rapid cooling method towards high-capacity vanadium nitride anode materials. Adv. Energy Mater. https://doi.org/10.1002/aenm.202103158.

Yao, Y., Wang, H., Yang, H., Zeng, S., Xu, R., Liu, F., Shi, P., Feng, Y., Wang, K., Yang, W., et al. (2020). A dual-functional conductive framework embedded with TiN-VN heterostructures for highly efficient polysulfide and lithium regulation toward stable Li–S full batterie. Adv. Mater. 32, 1905658.

Yu, J., Lu, W., Smith, J., Booksh, K., Meng, L., Huang, Y., Li, Q., Byum, J., Oh, Y., Yan, Y., et al. (2017). A high performance stretchable asymmetric fiber-shaped supercapacitor with a core-sheath helical structure. Adv. Energy Mater. 7, 1600976.

Yu, H., Deng, C., Yan, H., Xia, M., Zhang, X., Wang, Z., and Shu, J. (2021). Cu$_3$(PO$_4$)$_2$: novel anion convertor for aqueous dual-ion battery. Nanomicro Lett. 41, 7–14.

Zhang, Q., Wang, X., Pan, Z., Sun, J., Zhao, J., Zhang, J., Zhang, C., Tang, L., Luo, J., Song, B., et al. (2017). Wrapping aligned carbon nanotube composite sheets around vanadium nitride nanowire arrays for asymmetric coaxial fiber-

shaped supercapacitors with ultrahigh energy density. Nano Lett. 17, 2719–2726.

Zhang, R., Zhang, Y., Ren, X., Luo, Y., Cui, G., Asiri, A., Zheng, B., and Sun, X. (2018a). High-efficiency electrosynthesis of ammonia with high selectivity under ambient conditions enabled by VN nanosheet array. ACS Sustain. Chem. Eng. 6, 9545–9549.

Zhang, Z., Hu, X., Zhou, Y., Wang, S., Yao, L., Pan, H., Su, C., Chen, F., and Hou, X. (2018b). Aqueous rechargeable dual-ion battery based on fluoride ion and sodium ion electrochemistry. J. Mater. Chem. A 6, 8244–8250.

Zhang, Y., An, Y., Yin, B., Jiang, J., Dong, S., Dou, H., and Zhang, X. (2019). A novel aqueous ammonium dual-ion battery based on organic polymers. J. Mater. Chem. A 7, 11314–11320.

Zhang, Y., Chen, L., Hao, C., Zheng, X., Guo, Y., Chen, L., Lai, K., Zhang, Y., and Ci, L. (2020). Potassium pre-inserted K$_{1.04}$Mn$_8$O$_{16}$ as cathode materials for aqueous Li-ion and Na-ion hybrid capacitors. J. Energy Chem. 46, 53–61.

Zhao, D., Cui, Z., Wang, S., Qin, J., and Cao, M. (2016). VN hollow spheres assembled from porous nanosheets for high-performance lithium storage and the oxygen reduction reaction. J. Mater. Chem. A 4, 7914–7923.

Zheng, B., Huang, T., Kou, L., Zhao, X., Gopalsamy, K., and Gao, C. (2014). Graphene fiber-based asymmetric micro-supercapacitors. J. Mater. Chem. A 2, 9736–9743.

Zhu, M., Huang, Y., Huang, Y., Meng, W., Gong, Q., Li, G., and Zhi, C. (2015). An electrochromic supercapacitor and its hybrid derivatives: quantifiably determining their electrical energy storage by an optical measurement. J. Mater. Chem. A 3, 21321–21327.

STAR★METHODS

KEY RESOURCES TABLE

REAGENT or RESOURCE	SOURCE	IDENTIFIER
Chemicals, peptides, and recombinant proteins		
acetic acid	sigma Aldrich	CAS:64-19-7
hydrofluoric acid	sigma Aldrich	CAS:7664-39-3
potassium permanganate	sigma Aldrich	CAS:7722-64-7
hydrochloric acid	sigma Aldrich	CAS:7647-01-0
potassium hydroxide	sigma Aldrich	CAS:1310-58-3
sodium tetraborate	sigma Aldrich	CAS:1330-43-4
titanium foil	sigma Aldrich	CAS:7440-32-6
vanadium foil	sigma Aldrich	CAS:7440-62-2

RESOURCE AVAILABILITY

Lead contact

Further information and requests for resources and reagents should be directed to and will be fulfilled by the lead contact, Bo-Tian Liu (btliu2018@glut.edu.cn).

Materials availability

This study did not generate new unique reagents.

Data and code availability

- Data reported in this paper will be shared by the lead contact upon request.

- This paper does not report original code.

- Any additional information required to reanalyze the data reported in this paper is available from the lead contact upon request.

METHOD DETAILS

Materials

Acetic acid (CH_3COOH), vanadium foil, sodium tetraborate ($Na_2B_4O_7$), hydrofluoric acid (HF), metallic titanium foil, potassium permanganate ($KMnO_4$), hydrochloric acid (HCl), potassium hydroxide (KOH) were purchased from sigma Aldrich. The carbon cloth (W0S 1002 with thickness 360 μm) was purchased from Ce-Tech Co. Ltd. All regents were used as received without further purification, and all aqueous solutions were prepared with MilliQ water.

Synthesis of MPs VN electrode

The NPs V_2O_5 electrodes were *in situ* grown by anodizing (0.1mm thick) vanadium foil (99.9%) in a two-electrode configuration with vanadium foil (1 × 3 cm) and Pt foil (2 × 3 cm) as anode and cathode, respectively. Anodizing was carried out at 5°C in 50 mL solution of CH_3COOH (≥99.5%) with 0.001 mol $Na_2B_4O_7$ (≥99%) and 0.6 mL HF (≥40%). And, 0.001 mol metallic titanium was dissolved in the solution to introduce $[TiF_6]^{2-}$ ions in the electrolyte before anodizing process. The samples were anodized at a constant voltage of 100 V for 20 min, and then were transfer annealing at 200°C for 3 h in Ar. Subsequently, the MPs VN electrodes were prepared by calcining the obtained NPs V_2O_5 samples in a furnace under an NH_3 atmosphere at 550°C for 12 h.

Synthesis of $K_{2-x}Mn_8O_{16}$ NSs/CC electrode

$K_{2-x}Mn_8O_{16}$ NSs/CC electrodes were prepared by a simple hydrothermal method. Typically, 0.003 mol $KMnO_4$ and 1mL HCl (37%) were dissolved in 50mL deionized water and stirred for 20 min. Afterward, the obtained solution and carbon cloth (2 × 2 cm) were transferred to a 100 mL Teflon-lined autoclave,

and then sealed and heated for 2 h at 160°C. After naturally cooling the autoclave to room temperature, the carbon cloth was washed thoroughly three times with deionized water, and then was annealed at 200°C for 3 h in air.

Materials characterization

The crystallographic information and phase purity of the samples were investigated by X-ray diffraction (XRD, Rigaku D/MAX-2500) equipped with Cu-Kα radiation (λ = 0.15406 nm). The surface species and chemical states of the samples were measured by X-ray photoelectron spectroscopy (XPS, Thermo Fisher Scientific Escalab 250Xi) using an Al Kα X-ray source at 15 kV and 10 mA. The morphologies of the samples were characterized using scanning electron microscopy (SEM, Zeiss, 5.0–20.0 kV) with an EDX detector, fieldemission transmission electorn microscope (FE-TEM, JEOL JEM-2800, 200 keV) with an EDX detector.

Electrochemical measurements and calculations

Electrochemical measurements were performed on an electrochemical workstation (Iviumstat electro-chemical analyser, Ivium Technology) at room temperature. All as-prepared electrodes (1 × 1 cm) were directly used as the working electrode without extra current collector. The electrochemical properties of electrodes were studied in a three-electrode system, with a Pt foil as counter electrode and Ag/AgCl as reference electrode, in 1 M KOH aqueous electrolyte. To measure the electrochemical performance of RDHSC devices, it was assembled by $K_{2-x}Mn_8O_{16}$ NSs/CC cathode and MPs VN anode, and then performed on two-electrode configuration in 1 M KOH aqueous electrolyte. The electrochemical measurements including cyclic voltammetry curves, the galvanostatic charging-discharging profiles, and the electrochem-ical impedance spectroscopy were performed using an iviumstat electrochemical analyser.

The areal specific capacitance (C_S), areal energy density (E_S) and power density (P_S) from the charge/discharge curves can be calculated in terms of (Equations 1, 2, and 3):

$$C_S = \frac{I \cdot \Delta t}{S \cdot \Delta V} \quad \text{or} \quad C_S = \frac{\int i(V)dV}{2 \cdot S \cdot v \cdot \Delta V} \qquad \text{(Equation 1)}$$

$$E_S = \frac{C_S \cdot \Delta V^2}{2} \qquad \text{(Equation 2)}$$

$$P_S = \frac{E_S}{\Delta t} \qquad \text{(Equation 3)}$$

Where, I is the discharge current; Δt is the discharge time; ΔV is the potential window; S is the electrodes area; v is the scan rate.